Full Band Semi-Classical Monte-Carlo Simulation of Layer Number-Dependent Electron Transport in MoS_2 and InSe

Sukhyeong Youn
Department of Materials Science and Engineering
Yonsei University
Seoul 03722, South Korea
suknjong@yonsei.ac.kr

Donghyeok Lee
Department of Materials Science and Engineering
Yonsei University
Seoul 03722, South Korea
dju94@yonsei.ac.kr

Jiwon Chang*
Department of System Semiconductor Engineering
Yonsei University
Seoul 03722, South Korea
jiwonchang@yonsei.ac.kr

***Abstract*—Transport characteristics of two-dimensional (2D) materials such as MoS_2 and InSe exhibit strong dependence on the thickness, yet the detailed theoretical understanding remains incomplete. Here, we investigate intrinsic layer number -dependent electron transport properties by employing a combined first-principles and semi-classical full-band Monte-Carlo (SCMC) simulation framework. Electronic band structures and phonon-limited scattering rates are obtained from density functional theory (DFT) and density functional perturbation theory (DFPT), and subsequently incorporated into SCMC carrier transport simulations. For MoS_2, mobility remains nearly unchanged from monolayer to bilayer, but decreases significantly in trilayer due to enhanced intervalley scattering into low-mobility Q-valleys. Meanwhile, InSe exhibits a monotonic increase in mobility with increasing thickness, attributed to the reduced density of states and suppressed scattering. Despite a moderate reduction in saturation velocity at high electric fields, InSe consistently outperforms MoS_2 in terms of mobility. Valley-resolved drift velocities and populations are analyzed to elucidate the layer number-dependent behaviors of mobility and velocity saturation.**

Keywords—semi-classical Monte-Calro, first-principles, 2D materials, carrier transport

I. Introduction

In recent years, two-dimensional (2D) materials have attracted intense interest as channel materials for field-effect transistors (FETs), owing to the atomically thin thickness, high carrier mobilities [1,2], and potential to suppress short channel effects [3]. Such properties make 2D materials as promising alternatives to conventional semiconductors in deeply scaled, low-power electronics, where silicon channels face increasing challenges such as short-channel effects, leakage currents, and degraded electrostatic control. Among various 2D materials, transition metal dichalcogenides (TMDs) such as molybdenum disulfide (MoS_2) and tungsten disulfide (WS_2) have been extensively studied as n- and p-channel materials, respectively. In addition, indium selenide (InSe) has also demonstrated excellent n-type FETs performance [4], highlighting the potential as a high-performance n-channel material. Experimentally measured mobilities of MoS_2 and InSe have been reported to range from 100 to over 1000 $cm^2/V \cdot s$, depending on various factors such as substrate choice, encapsulation, and interface quality [5,6]. In particular, bilayer and trilayer MoS_2 often exhibit higher carrier mobility than the monolayer, highlighting the roles of interlayer coupling and electrostatic screening [7]. Similar trends have been reported for InSe, although systematic investigations across different thicknesses and crystal phase remain limited. Despite these experimental observations, a fundamental theoretical understanding of electron mobility scales with thickness remains incomplete.

In this work, we investigate carrier transport in MoS_2 and InSe using semi-classical Monte Carlo simulations to evaluate transport characteristics under substrate-free conditions. Through a comparative analysis of monolayer, bilayer, and trilayer structures, we examine the impact of thickness on drift velocity and low-field mobility. Our results reveal that InSe exhibits consistently higher mobility than MoS_2, with the performance gap widening as the number of layers increases, underscoring the suitability of InSe as a scalable 2D channel material for high-performance nanoelectronic applications.

II. Methods

Density functional theory (DFT) and density functional perturbation theory (DFPT) calculations were carried out using the Quantum ESPRESSO package [10], with the Perdew–Burke–Ernzerhof generalized gradient approximation (GGA-PBE) [11] for the exchange–correlation functional. Optimized norm conserving Vanderbilt pseudopotentials (ONCV) [12] were employed for all atomic elements. All structures included a vacuum layer to remove the spurious interactions between periodic structures and were geometrically optimized by minimizing the total energy with respect to atomic positions and lattice parameters. Computational parameters are summarized in Table 1.

Both the electronic band structure and the electron-phonon scattering rates were obtained via maximally localized Wannier interpolation implemented in the Electron–Phonon Wannier (EPW) package [13]. These were first calculated on a coarse k-point mesh of 12×12×1 and a q-point mesh of 6×6×1, then interpolated onto finer grids: a k-point mesh of 200×200×1 for the band structure and 80×80×1 meshes for both k and q in the scattering rate calculations using Fermi's golden rule.

Full-band cellular Monte-Carlo (CMC) simulations were conducted using band structures and electron–phonon scattering rates obtained through the first-principles workflow

TABLE I. Input Parameters Used for Quantum Espresso Calculations

Parameters	Values
Kinetic energy (E_k) cutoff	60 Ry
Charge density cutoff	240 Ry
Ionic minimization threshold	10^{-6} Ry
Self-consistent field threshold	10^{-12} Ry

This research was supported by the MOTIE (Ministry of Trade, Industry & Energy) (1415185352) and KSRC (Korea Semiconductor Research Consortium) (20019450) support program for the development of the future semiconductor device. This work was also supported by the Technology Innovation Program ("RS-2023-00234828") funded by the Ministry of Trade, Industry & Energy (MOTIE, Korea) (1415187391).

described above, including DFT, DFPT, and Wannier-based interpolation. Initial carrier distributions were stochastically sampled according to the Fermi–Dirac distribution at 300 K. An ensemble of 100,000 electrons was simulated with a time step of 0.02 ps. At each electric field (*E*-field), convergence of the drift velocity was determined by comparing 400 steps and 200 steps moving averages; iterations continued until the relative error between the two averages fell below 0.1 %.

III. Results & Discussion

Fig. 1 presents the electronic band structures and phonon dispersions of monolayer, bilayer, and trilayer MoS_2 and InSe, obtained from DFT calculations and plotted along the high-symmetry *k*-points of the hexagonal Brillouin zone. These results are in excellent agreement with prior first-principles studies [9,15]. For MoS_2, the lowest conduction band valley (K-valley) is at K-point while the 2nd lowest valley (Q-valley) is at Q-point between Γ- and K-points. The energy separations (ΔE_{QK}) between K- and Q-valleys are 274 meV, 215 meV, and 72 meV for monolayer, bilayer, and trilayer, respectively. For InSe, the lowest conduction band valleys (Γ-valley) and the 2nd lowest conduction band valleys (M-valley) are observed at Γ- and M-points, respectively. The energy separations from Γ to M ($\Delta E_{\Gamma M}$) are 711 meV, 762 meV, and 840 meV for monolayer, bilayer, and trilayer respectively. The energy separations from the 1st Γ to the 2nd Γ (ΔE_{Γ}) are 355 meV, and 569 meV for bilayer, and trilayer respectively.

Fig. 2 shows the drift velocities of monolayer, bilayer, and trilayer of MoS_2 and InSe as a function of *E*-field. The simulation results for monolayer are in good agreement with previously reported simulations [8,14]. The extracted mobilities are listed in Table 2. They were obtained by evaluating the slope of drift velocity *vs*. *E*-field curve in the low-field region. In the case of MoS_2, monolayer and bilayer exhibit similar mobilities, while trilayer shows lower mobility. On the other hand, for InSe, the mobility tends to increase as the number of layers increases. For all cases, the drift velocity either saturates or decreases with increasing *E*-field in the high-field region.

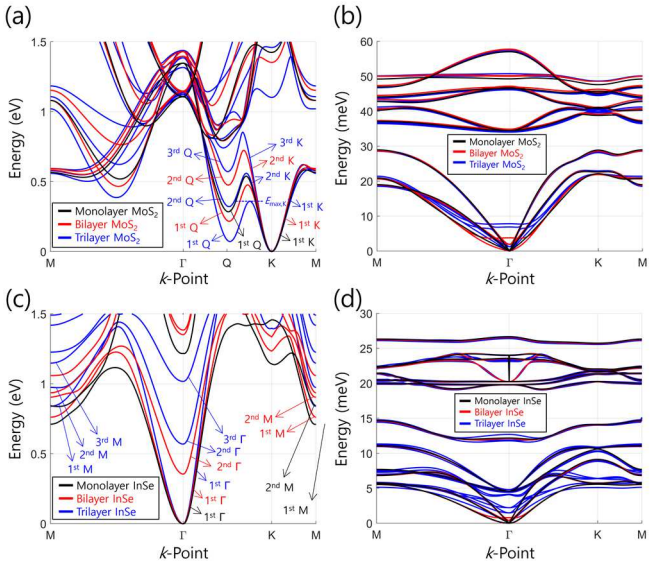

Fig. 1. (a) Conduction band structures and (b) phonon band structures of monolayer, bilayer, and trilayer MoS_2 along the high-symmetric points in the 1st Brillouin zone. (c) Conduction band structures and (d) phonon band structures of monolayer, bilayer, and trilayer InSe along the high-symmetric points in the 1st Brillouin zone.

To understand different behaviors of drift velocity *vs*. *E*-field in Fig. 2, we investigated the valley-resolved drift velocity and population of each valley at different *E*-field. Fig. 3 shows the drift velocity and population in each valley for monolayer, bilayer, and trilayer MoS_2, respectively. At low *E*-field (< 10^4 V/cm), monolayer and bilayer exhibit nearly identical velocities (Figs. 3a, and 3c) as all carriers occupy K-valleys (Figs. 3b, and 3d), which have similar band curvatures as seen in the band structure in Fig. 1a. In contrast, for trilayer, the small ΔE_{QK} results in a substantial valley population in the 1st Q-valley (Fig. 3f), leading to the lower drift velocity compared to monolayer and bilayer in Fig. 2a. As *E*-field increases, both monolayer and bilayer exhibit drift velocities approaching the respective peak values at similar *E*-field. Therefore, $E_{0.9peak}$ defined as the *E*-field at which the drift velocity reaches 90 % of the maximum value, as shown in Figs. 3a and 3c, is similar for both monolayer and bilayer. This behavior can be attributed to the onset of intervalley scattering from the K-valley into the 1st Q-valley, as illustrated in Figs. 3b and 3d, and is in qualitative agreement with previous studies [15]. In trilayer, however, $E_{0.9peak}$ is higher (Fig. 3e) than monolayer and bilayer. Since the 1st Q-valley already holds a substantial fraction of carriers at low *E*-field, velocity saturation is mainly governed by scattering into both the 1st and 2nd Q-valleys, whose populations increase more rapidly at higher *E*-field. At higher *E*-field (~10^6 V/cm), drift velocity of the carriers in K-valley decreases in all cases. The decline is the steepest for the 1st K-valley in trilayer (Fig. 3e) since carriers reach the energy peak ($E_{max,K}$) region between K- and Q-valleys in Fig. 1a, where the effective mass dramatically increases. For trilayer, energy-resolved carrier distribution with velocity in Fig. 4 confirms that a larger fraction of carriers occupies states near $E_{max,K}$, which drives the rapid suppression of K-valley drift velocity.

Fig. 5 shows the drift velocity and valley population in monolayer, bilayer, and trilayer InSe as a function of *E*-field. As the layer number increases, the drift velocity in the low-field region also increases. This enhancement in mobility is primarily attributed to the increased curvature of the Γ-valley in Fig. 1c, which leads to a reduced effective mass and, consequently, a lower density of states (DOS), as shown in Fig. 6. The decrease in DOS limits the number of available final

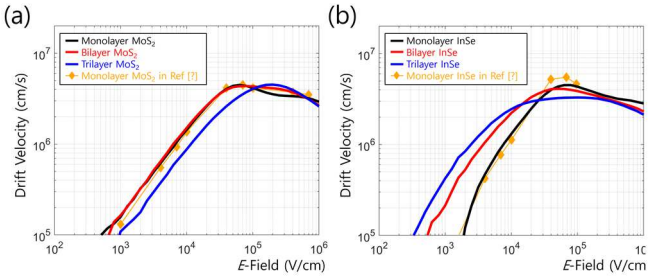

Fig. 2. Drift velocity of carriers as a function of *E*-field for monolayer (black), bilayer (red), and trilayer (blue) MoS_2 and InSe, respectively. Previously reported calculations for monolayer MoS_2 and InSe from [8,14] are included for comparison (orange symbols).

TABLE II. Electron Mobility of MoS_2 and InSe According to Layer Number

MoS_2	Mobility (cm^2/Vs)	InSe	Mobility (cm^2/Vs)
Monolayer	146	Monolayer	159
Bilayer	151	Bilayer	277
Trilayer	97.2	Trilayer	463

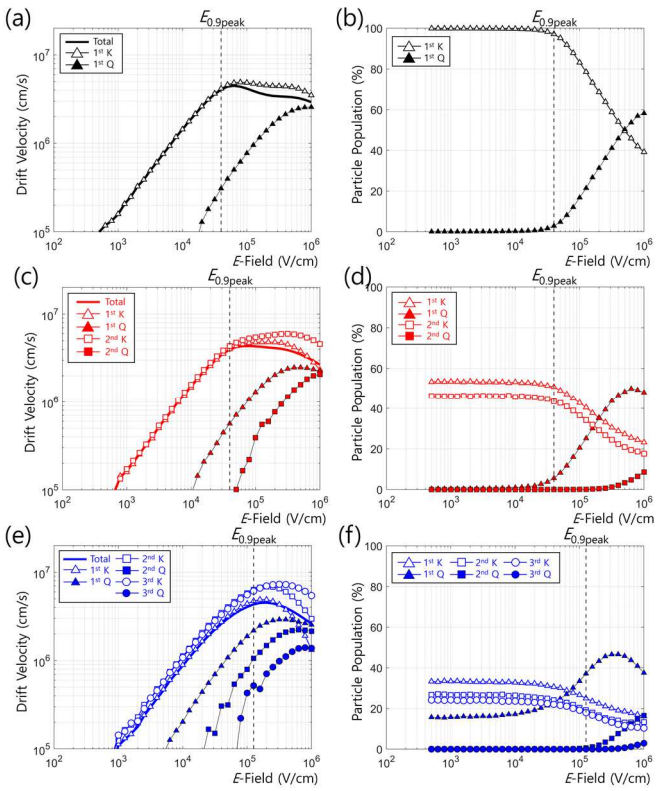

Fig. 3. Drift velocity of total carriers, carriers in K- and Q-valleys and valley population of K- and Q-valleys as a function of E-field for monolayer ((a) and (b)), bilayer ((c) and (d)), and trilayer ((e) and (f)) MoS_2.

states for electron–phonon scattering, thereby suppressing scattering rates and enabling higher drift velocities. While reduced electron–phonon scattering enhances low-field mobility, increasing E-field drives carriers to higher energy states, where intervalley scattering becomes more significant. In monolayer InSe, carriers begin to populate the M-valley, whereas in bilayer and trilayer, scattering into the 2nd Γ-valley is more pronounced as shown in Figs. 5b, 5d, and 5f. Notably, the population of the 2nd Γ-valley is slightly higher in trilayer than in bilayer InSe, even at low E-fields. This trend is clarified in Fig. 7, which presents the energy-resolved carrier distributions in bilayer and trilayer InSe at E-field of 10^3 V/cm. As shown in Figs. 7b and 7d, trilayer carriers exhibit a broader

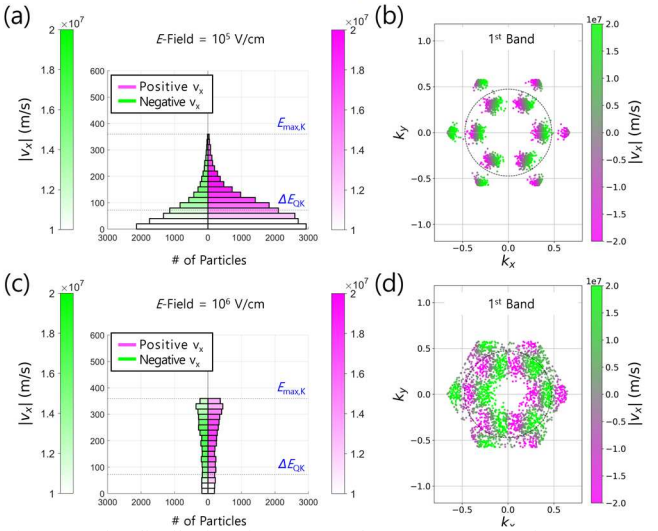

Fig. 4. Carrier distributions in energy and momentum space for carriers in the 1st K-valley of trilayer MoS_2 at E-field of 10^5 V/cm ((a) and (b)) and 10^6 V/cm ((c) and (d)), respectively. Boundary between K- and Q-valleys are indicated by black circles in (b) and (d). The size of velocity is also represented by the color scale.

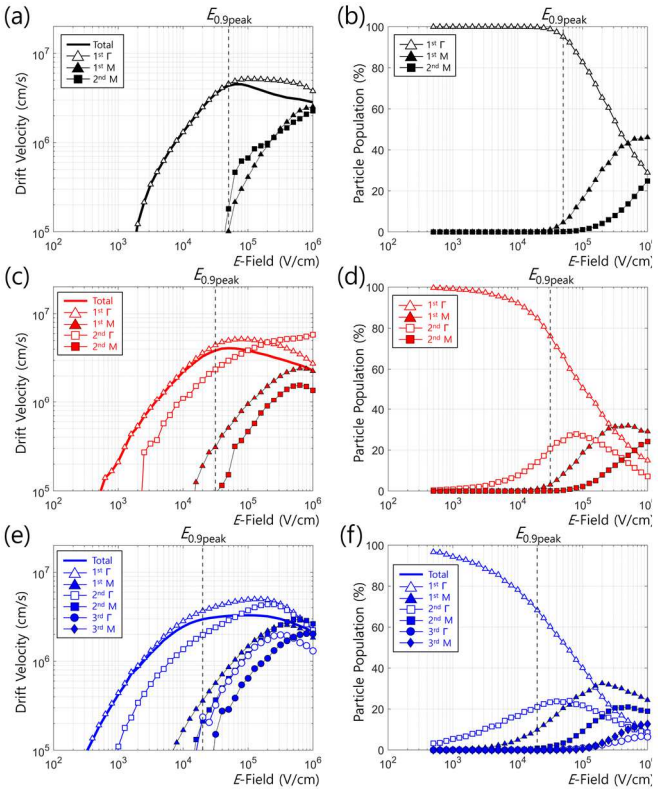

Fig. 5. Drift velocity of total carriers, carriers in Γ- and M-valleys and valley population of Γ- and M-valleys as a function of E-field for monolayer ((a) and (b)), bilayer ((c) and (d)), and trilayer ((e) and (f)) InSe.

distribution in k-space, corresponding to a higher average kinetic energy (Figs. 7a and 7c). This broader distribution can also be attributed to the reduced DOS, which leads to suppressed electron–phonon scattering and allows carriers to retain higher energy. In contrast to the enhancement of low-field mobility, the saturation velocity decreases with increasing layer number. This behavior is primarily attributed to the more rapid depletion of the 1st Γ-valley, which contributes most significantly to high-velocity carriers. As the layer number increases, DOS of the 1st Γ-valley decreases due to the increased curvature of the Γ-valley as confirmed in Fig. 6, which in turn suppresses electron–phonon scattering. This reduction in scattering allows carriers to retain energy more effectively, resulting in a higher average kinetic energy and a broader distribution in k-space. Consequently, they are more likely to occupy higher-energy valleys and escape from the 1st Γ-valley, leading to an earlier onset of saturation. At $E_{0.9peak}$,

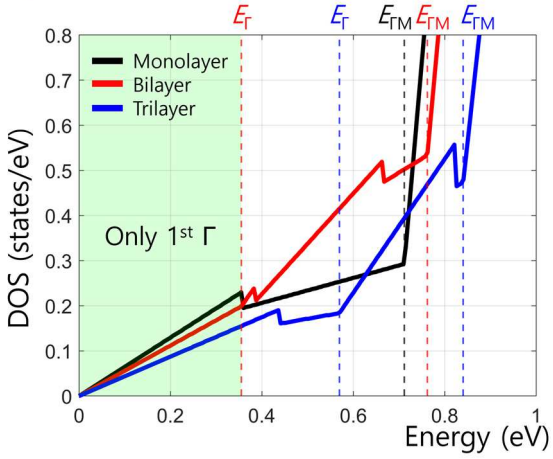

Fig. 6. Density of states (DOS) as a function of energy for monolayer (black), bilayer (red), and trilayer (blue) InSe.

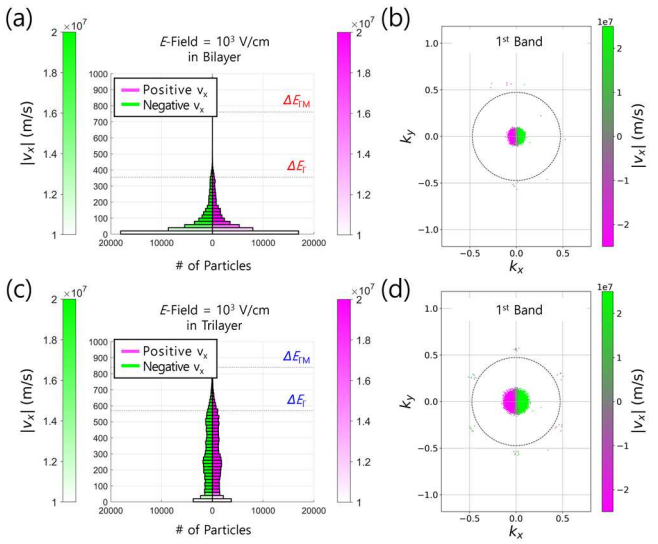

Fig. 7. Carrier distributions in energy and momentum space for carriers in the 1st Γ-valley of bilayer InSe ((a) and (b)) and trilayer InSe ((c) and (d)), respectively, at E-field of 10^3 V/cm. Boundary between Γ- and M-valleys are indicated by black circles in (b) and (d). The size of velocity is also represented by the color scale.

the population in the 1st Γ-valley drops to 95.2%, 76.1%, and 68.3% for monolayer, bilayer, and trilayer InSe, respectively, indicating enhanced intervalley scattering in thicker layers.

IV. Conclusion

In this work, we performed a comparative analysis of electron transport in MoS_2 and InSe using full band SCMC simulations combined with first-principles calculations. The layer number dependence of electron mobility and velocity saturation is examined through valley-resolved drift velocities and carrier populations. Our results reveal distinct thickness-dependent transport behaviors in MoS_2 and InSe. In MoS_2, both drift velocity and mobility remain nearly unchanged from monolayer to bilayer but decrease sharply in the trilayer, primarily due to enhanced intervalley scattering into the Q-valleys. In contrast, InSe exhibits a monotonic increase in mobility with increasing thickness, attributed to reduced effective mass and scattering rates resulting from a lower DOS.

References

[1] J.-H. Chen, C. Jang, S. Xiao, M. Ishigami, and M. S. Fuhrer, "Intrinsic and extrinsic performance limits of graphene devices on SiO_2," Nat. Nanotechnol., vol. 3, pp. 206–209, Mar. 2008.

[2] L. Li et al., "Black phosphorus field-effect transistors," Nat. Nanotechnol., vol. 9, pp. 372–377, Mar 2014.

[3] F. Schwierz, J. Pezoldt, and R. Granzner, "Two-dimensional materials and their prospects in transistor electronics," Nanoscale, vol. 7, no. 18, pp. 8261–8283, Apr. 2015.

[4] Y. Seok et al., "High-field electron transport and high saturation velocity in multilayer indium selenide transistors," ACS Nano, vol. 18, no. 11, pp. 8099–8106, Mar. 2024.

[5] B. Radisavljevic, A. Radenovic, J. Brivio, V. Giacometti, and A. Kis, "Single-layer MoS_2 transistors," Nat. Nanotechnol., vol. 6, pp. 147–150, Jan. 2011.

[6] Z. Li et al., "Enhancement of carrier mobility in multilayer InSe transistors by van der Waals integration," Nanomaterials, vol. 14, no. 4, p. 382, Feb. 2024.

[7] S. Ghatak, A. N. Pal, and A. Ghosh, "Nature of electronic states in atomically thin MoS_2 field-effect transistors," ACS Nano, vol. 5, no. 10, pp. 7707–7712, Sep. 2011.

[8] S. Gopalan, G. Gaddemane, M. L. Van de Put, and M. V. Fischetti, "Monte Carlo study of electronic transport in monolayer InSe," Materials, vol. 12, no. 24, p. 4210, Dec. 2019.

[9] D. K. Sang et al., "Two dimensional β-InSe with layer-dependent properties: Band alignment, work function and optical properties," Nanomaterials, vol. 9, no. 1, p. 82, Jan. 2019.

[10] P. Giannozzi et al., "QUANTUM ESPRESSO: A modular and open-source software project for quantum simulations of materials," *J. Phys. Condens. Matter*, vol. 21, no. 39, pp. 395502, Sep. 2009.

[11] J. P. Perdew, K. Burke, and M. Ernzerhof, "Generalized gradient approximation made simple," Phys. Rev. Lett., vol. 77, no. 18, pp. 3865–3868, Oct. 1996.

[12] D. R. Hamann, "Optimized norm-conserving Vanderbilt pseudopotentials," Phys. Rev. B, vol. 88, no. 8, pp. 085117, Aug. 2013.

[13] S. Poncé, E. R. Margine, C. Verdi, and F. Giustino, "EPW: Electron–phonon coupling, transport and superconducting properties using maximally localized Wannier functions," Comput. Phys. Commun., vol. 209, pp. 116–133, Dec. 2016.

[14] S. Gopalan, S. Mansoori, M. Van de Put, G. Gaddemane, and M. Fischetti, "Monte Carlo study of carrier transport in two-dimensional transition metal dichalcogenides: high-field characteristics and MOSFET simulation," J. Comput. Electron., vol. 22, pp. 1240–1256, Jul. 2023.

[15] C. Zhang, L. Cheng, and Y. Liu, "Understanding high-field electron transport properties and strain effects of monolayer transition metal dichalcogenides," Phys. Rev. B, vol. 102, p. 115405, Sep. 2020.